Particle deposition in a realistic geometry of the human conducting airways: Effects of inlet velocity profile, inhalation flowrate and electrostatic charge

Effects of inlet velocity profile, inhalation flowrate and electrostatic charge

Koullapis, P. G.; Kassinos, S. C.; Bivolarova, Mariya Petrova; Melikov, Arsen Krikor

Published in:
Journal of Biomechanics

Link to article, DOI:
10.1016/j.jbiomech.2015.11.029

Publication date:
2016

Document Version
Publisher's PDF, also known as Version of record

Journal of Biomechanics 49 (2016) 2201–2212

Contents lists available at ScienceDirect

Journal of Biomechanics

journal homepage: www.elsevier.com/locate/jbiomech
www.JBiomech.com

Particle deposition in a realistic geometry of the human conducting airways: Effects of inlet velocity profile, inhalation flowrate and electrostatic charge

P.G. Koullapis [a], S.C. Kassinos [a,*], M.P. Bivolarova [b], A.K. Melikov [b]

[a] Computational Sciences Laboratory (UCY-CompSci), Department of Mechanical and Manufacturing Engineering, University of Cyprus, Kallipoleos Avenue 75, Nicosia 1678, Cyprus
[b] International Centre for Indoor Environment and Energy, Technical University of Denmark, Building 402, 2800 Lyngby, Denmark

ARTICLE INFO

Article history:
Accepted 11 November 2015

Keywords:
Computational fluid-particle dynamics simulation
Large eddy simulation
Aerosol deposition in the human upper airways
Steady inhalation
Inlet conditions
Electrostatic image charge force

ABSTRACT

Understanding the multitude of factors that control pulmonary deposition is important in assessing the therapeutic or toxic effects of inhaled particles. The use of increasingly sophisticated in silico models has improved our overall understanding, but model realism remains elusive. In this work, we use Large Eddy Simulations (LES) to investigate the deposition of inhaled aerosol particles with diameters of $d_p = 0.1$, 0.5, 1, 2.5, 5 and 10 μm (particle density of 1200 kg/m^3). We use a reconstructed geometry of the human airways obtained via computed tomography and assess the effects of inlet flow conditions, particle size, electrostatic charge, and flowrate. While most computer simulations assume a uniform velocity at the mouth inlet, we found that using a more realistic inlet profile based on Laser Doppler Anemometry measurements resulted in enhanced deposition, mostly on the tongue. Nevertheless, flow field differences due to the inlet conditions are largely smoothed out just a short distance downstream of the mouth inlet as a result of the complex geometry. Increasing the inhalation flowrate from sedentary to activity conditions left the mean flowfield structures largely unaffected. Nevertheless, at the higher flowrates turbulent intensities persisted further downstream in the main bronchi. For $d_p > 2.5$ μm, the overall Deposition Fractions (DF) increased with flowrate due to greater inertial impaction in the oropharynx. Below $d_p = 1.0$ μm, the DF was largely independent of particle size; it also increased with flowrate, but remained significantly lower. Electrostatic charge increased the overall DF of smaller particles by as much as sevenfold, with most of the increase located in the mouth–throat. Moreover, significant enhancement in deposition was found in the left and right lung sub-regions of our reconstructed geometry. Although there was a relatively small impact of inhalation flowrate on the deposition of charged particles for sizes $d_p < 2.5$ μm, impaction prevailed over electrostatic deposition for larger particles as the flowrate was increased. Overall, we report a significant interplay between particle size, electrostatic charge, and flowrate. Our results suggest that in silico models should be customized for specific applications, ensuring all relevant physical effects are accounted for in a self-consistent fashion.

1. Introduction

Aerosol particle deposition in the airways depends on several parameters, such as the physical and hydrodynamic characteristics of the particles themselves, the inhalation flowrate, the health state of the individual and the geometrical and morphological details of the airways. A considerable amount of investigative effort in terms of experiments and numerical simulations has been directed at determining deposition efficiencies. Early studies have afforded us a satisfactory level of understanding of general trends in deposition efficiencies as a function of particles sizes. They have also improved our understanding of the airflow characteristics. For example, today we have a much better appreciation of the effects of flow turbulence in the conducting airways than we did 20 years ago (Kleinstreuer and Zhang, 2010; Lin et al., 2013). Yet, this overall understanding falls short of the precision one needs when optimizing pharmaceutical products consisting of inhaler-formulation pairs or when establishing links of particular pollutants to specific disease pathways in the airways. To complicate matters further, anatomical variations between individuals, which can be either hereditary or due to disease-induced airway remodeling, alter

* Corresponding author.
E-mail address: kassinos@ucy.ac.cy (S.C. Kassinos).

http://dx.doi.org/10.1016/j.jbiomech.2015.11.029

deposition to a degree that is modulated by particle size and charge, flowrate, and other factors.

In vivo studies of aerosol deposition in the human lungs are limited by concerns over human safety and by resolution limitations of current imaging technologies. In silico models based on Computational Fluid Dynamics (CFD) can fill this gap by providing an unprecedented level of detail that would allow scientists and engineers to experiment with alternate designs and conditions.

Recent studies revealed the unsteady and turbulent nature of the flow in regions downstream of the glottis, with turbulent effects dissipating only in the deeper conducting airways where the local Reynolds number decreases gradually (Kleinstreuer and Zhang, 2010; Tawhai and Lin, 2011). There are three techniques for solving turbulent flow equations using a computer: direct numerical simulations (DNS), Reynolds averaged Navier–Stokes (RANS) and large eddy simulations (LES). DNS tracks the details of the instantaneous turbulent fluctuations at all scales, however, it is exceedingly costly to implement and beyond routine use on current computers. Presently, most CFD simulations solve only for the mean flow using the RANS equations, resulting in a tremendous reduction in computational cost. However, the laminar-turbulent-laminar flow transition in the conducting airways is challenging for RANS and care must be exercised to choose validated RANS models (Xi and Longest, 2007). A more robust choice is the method of Large Eddy Simulations (LES), where the smallest scales of motion (containing a small fraction of the kinetic energy) are discarded. The computational expense of LES is considerably higher than that of RANS, but it retains significantly more elements of the underlying turbulence physics than RANS (Choi et al., 2009; Radhakrishnan and Kassinos, 2009). With constant gains in computing power, LES has become affordable for routine use and recent LES-based deposition studies have established the trustworthiness of the method.

In the case of inhaled pollutants, ambient conditions such as the air and aerosol characteristics in the breathing zone of an occupant can be expected to play a role in determining deposition in the airways. Longest et al. (2008) investigated the deposition characteristics of ambient and capillary-generated spray aerosols in a realistic mouth–throat geometry. They found that spray momentum effects induce significantly more deposition than ambient aerosols, especially in the first section of the mouth–throat geometry as a result of spray inertia interacting with the tongue. In the absence of a free stream airflow (e.g. as caused by a ventilation system), the air flowfield in the breathing zone results from the interaction between the occupant's breath with a free convection flow around the body. Temperature differences between the body surface and the surrounding air drive the free convective flow, which starts slow and laminar with a thin boundary layer at the lower parts of the body, but becomes faster and turbulent with a thick boundary layer at the height of the head (Lewis et al., 1969; Licina et al., 2014). Airborne particles close to the ground can be transported by the convective flow into the breathing zone, a process that has a potentially negative impact on the quality of the inhaled air (Licina et al., 2015a,b). Aerosols and air parcels are transported by the free convective flow with sufficient momentum and turbulence intensities to alter the characteristics of the flowfield in the pharyngeal cavities during inhalation, but these effects remain largely unexplored.

A second important determinant of deposition is the respiratory flowrate, which is crucial during the patient initiated maneuver for inhaling medicines, but also during exposure to environmental pollutants. Flowrates of 15, 30 and 60 l/min are considered to correspond to sedentary, light and heavy activity conditions (Xi and Longest, 2007), while in the cases of rapid inhalation, typically encountered during the use of pharmaceutical aerosol inhalation devices, inhalation flowrate can reach values up to 120 l/min (Johnstone et al., 2004). A higher flowrate causes earlier transition to turbulence in the upper airways and the ensuing fluctuations make aerosol particles move erratically, thus altering deposition patterns in a size-dependent fashion. Also, turbulence produced in the oropharynx can be advected to several generations of the tracheobronchial tree, as estimated in Finlay (2001), for a simplified cylinder-based airway model and for airflow Reynolds numbers above 2000 in the larynx.

Electrostatic charge carried by inhaled particles is also an important determinant of deposition, especially in the case of drug delivery. Medical devices such as nebulisers, Metered Dose Inhalers (MDI) and Dry Powder Inhalers (DPI) often generate electrostatically charged aerosols (Byron et al., 1997; Kwok et al., 2005). But even environmental aerosols may have charges well above the Boltzmann equilibrium and thus electrostatic charge must be taken into account in human health risk assessments (Forsyth et al., 1998). Several theoretical studies in lung models (Yu, 1985; Bailey et al., 1998), experiments in man (Melandri et al., 1983; Prodi and Mularoni, 1985) as well as clinical measurements confirmed that charge carried by particles enhances the deposition of the particles in the lung considerably. This is not desirable for drugs intended for systemic uptake, which must pass into circulation through the alveolar epithelium, but might be desirable for drug delivery in certain upper regions of the airway tree or even leveraged for the removal of pollutant particles using electrostatic charge effects (Ali et al., 2008).

In this work, we use LES to study the effects of the mouth inlet velocity profile and of electrostatic charge at various inhalation flowrates on particle deposition patterns inside a realistic model of the human upper airways. Specifically, two different inlet conditions are examined under steady inhalation at a flowrate of 4.5 l/min. The first is a uniform velocity profile, as used in most current computational studies. The second is a velocity profile measured by us in the breathing zone of a breathing thermal manikin using Laser Doppler Anemometry (LDA), which is closer to the real case. The experiments to generate the measured profile are beyond the scope of the present paper and will be described in a separate publication. The effect of inhalation flowrate is examined by considering flowrates of 15, 30 and 60 l/min, while assuming uniform inlet velocity. Finally, deposition enhancement in the lungs due to electrostatic effects is also assessed as a function of inhalation flowrate.

2. Methods

2.1. Airway geometry

Early in silico models relied on simplified representations of the human airways, with many of them employing the symmetric model of Weibel (1963). Recent advancements in medical imaging have afforded us detailed views of the complex structures of the lung. The geometry considered in this study, (see Fig. 1(a) and (b) – coordinate system is also shown) is reconstructed from Multi-Detector Computed Tomography (MDCT) scans and it represents a non-smoking 20 year old female. This geometry was provided to us by the Department of Mechanical and Industrial Engineering of the University of Iowa (USA) and was also used in the study of Choi et al. (2009), where more details regarding the MDCT reconstruction method and the airway dimensions can be found. The respiratory tract includes the extrathoracic airways of the mouth, the oropharynx, the laryngopharynx, the larynx and the trachea as well as the intrathoracic airways up to generation 7. Table 1 summarizes the geometrical features of the reconstructed airways (average cross sectional area A and corresponding hydraulic diameter D_h) along with the key flow parameters (bulk velocity U and Reynolds number Re) for the three higher flowrates considered in this study.

When studying the effect of different velocity profiles imposed at the mouth inlet, the airway geometry is truncated at the end of the trachea in order to reduce the mesh size and computational cost. This simplification is based on preliminary numerical experiments that had shown that all differences in the flowfield due to inlet conditions dissipate in the upper airways and well before the flow reaches the tracheal bifurcation. Also, in order to match the velocity profile measured at the

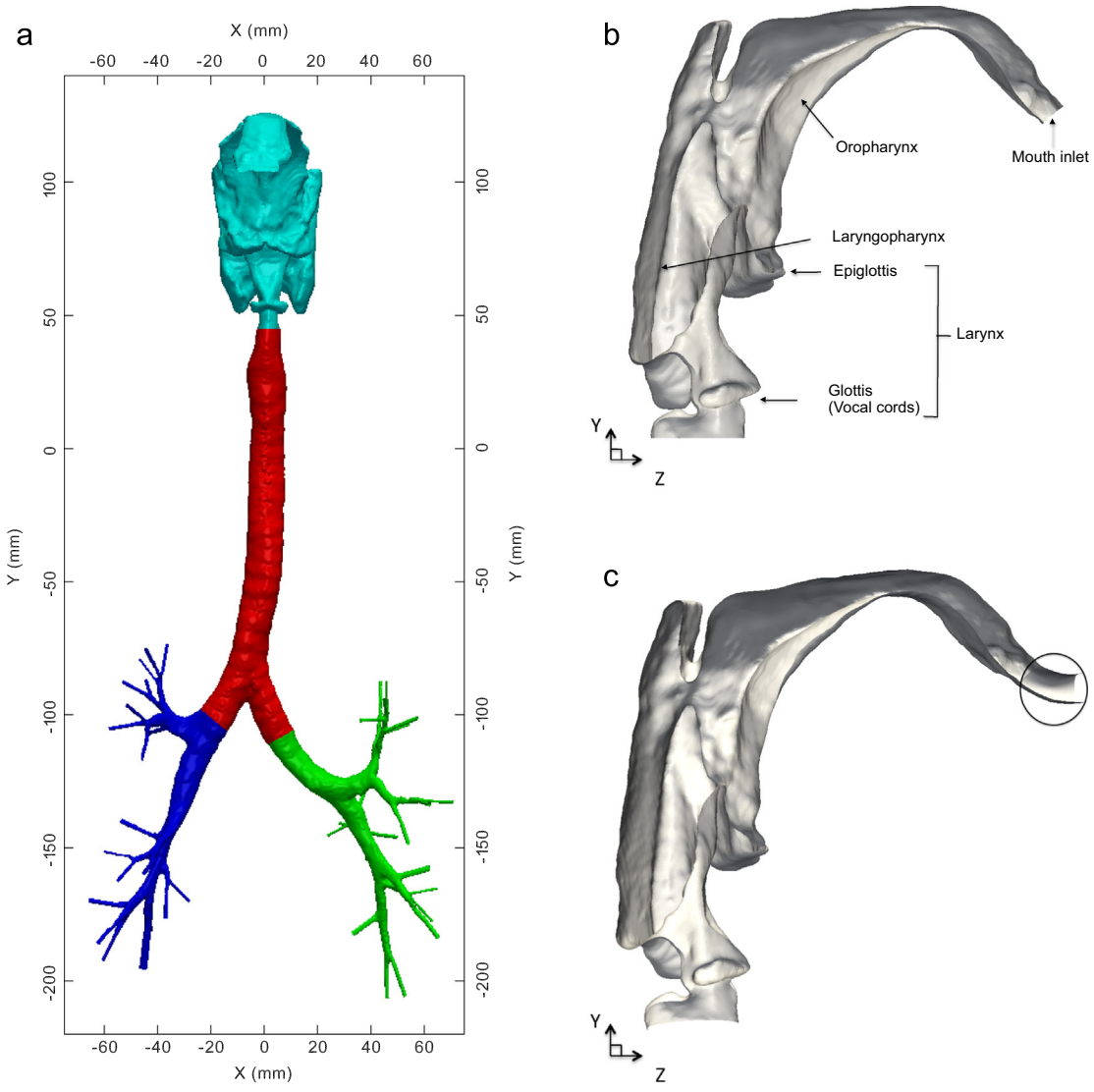

Fig. 1. Realistic human upper airways geometry (Choi et al., 2009). (a) Full geometry and sub-regions, i.e. mouth–throat (cyan), trachea (red), left (green) and right lung (blue). (b) Inside side view of the upper airways. (c) Modified airway geometry used in the case of different inlet velocity profiles (extruded part in the mouth inlet section in circle). The coordinate system is also shown. (For interpretation of the references to color in this figure caption, the reader is referred to the web version of this paper.)

Table 1
Geometrical and flow properties on the cross-sections of interest.

Cross section	**A** (mm^2)/ $\mathbf{D_h}$ (mm)	$\mathbf{U} = \frac{Q}{A}$ (m/s) $\dot{Q} = 15.2/30/60\ l/min$	$\mathbf{Re} = \frac{UD}{\nu} = \frac{2Q}{\nu\sqrt{\pi A}}$ $\dot{Q} = 15.2/30/60\ l/min$
Midpharynx	401 / 22.6	0.630 / 1.247 / 2.494	838 / 1654 / 3308
Glottis	39.3 /7.074	6.43 / 12.725 / 25.45	2676 / 5084 / 10,168
Trachea	157.8 / 14.2	1.6 / 3.17 / 6.34	1337 / 2639 / 5278

breathing zone of the breathing thermal manikin with the mouth inlet of the airway model, the initial geometry (Fig. 1(a)) was extruded slightly in the mouth inlet section as shown in Fig. 1(c).

2.2. Continuous phase simulation

We are employing Large Eddy Simulations (LES) using the dynamic version of the Smagorinsky–Lilly subgrid scale model (Lilly, 1992) in order to study the unsteady flow in the realistic human airway geometry. Previous studies have confirmed the ability of this model to deal with transitional flows (Tan et al., 2011; Radhakrishnan and Kassinos, 2009). The airflow is described by the filtered set of incompressible Navier–Stokes equations (Eqs. (1) and (2)) which are solved using OpenFOAM,

$$\frac{\partial \overline{u}_j}{\partial x_j} = 0 \tag{1}$$

$$\frac{\partial \overline{u}_i}{\partial t} + \overline{u}_j \frac{\partial \overline{u}_i}{\partial x_j} = -\frac{1}{\rho}\frac{\partial \overline{p}}{\partial x_i} + \frac{\partial}{\partial x_j}\left[(\nu + \nu_{sgs})\frac{\partial \overline{u}_i}{\partial x_j}\right]. \tag{2}$$

Here, $\overline{u}_i$, $\overline{p}$, $\rho = 1.2\ kg/m^3$, $\nu = 1.7 \times 10^{-5}\ m^2/s$ and ν_{sgs} are the velocity component in the i-direction, pressure, density and kinematic viscosity of air and subgrid scale (SGS) turbulent eddy viscosity, respectively. The overbar denotes resolved quantities.

The discretization of the equations is done using the finite volume method and second order schemes in both time and space. To ensure numerical stability the time steps used were 10, 5, 2.5 and 1×10^{-6} s for the cases of 4.5, 15.2, 30 and 60 l/min, respectively. Two unstructured hybrid meshes with 23 (Mesh 1) and 34 (Mesh 2) million control volumes were generated using the ANSYS ICEM software. Details of the generated meshes as well as a mesh sensitivity study are described in the Supplementary Methods. In all the simulation cases, zero pressure at the outlets was set as boundary conditions (Luo and Liu, 2008).

2.3. Lagrangian particle tracking

Spherical, rigid and non-rotating particles are introduced at the mouth inlet. The motion of each particle is individually computed (Lagrangian approach) by solving Newton's equations to determine the particle velocity ($\vec{u}_p$) and position

$(\vec{x}_p)$,

$$m_p\frac{d\vec{u}_p}{dt}=\vec{F}_D+\vec{F}_G+\vec{F}_B+\vec{F}_{\text{image}},\quad \frac{d\vec{x}_p}{dt}=\vec{u}_p. \tag{3}$$

The forces acting on each particle include sphere drag ($\vec{F}_D$), gravity ($\vec{F}_G=m_p\vec{g}$ where $\vec{g}=(0,-9.81\ \text{m/s}^2,0)$ is the gravitational acceleration vector), Brownian ($\vec{F}_B$) and electrostatic image charge forces ($\vec{F}_{\text{image}}$).

The expression for the drag force is based on the correlation proposed by Schiller and Naumann (1935),

$$\vec{F}_D=\frac{m_p}{\tau_p}(\vec{u}-\vec{u}_p), \tag{4}$$

where m_p is the mass of an individual particle, $\vec{u}$ is the filtered fluid velocity interpolated to the position of the particle and $\tau_p=(\rho_p d_p^2 C_c)/(18\mu_f C_D\frac{Re_p}{24})$ is the particle response time with $\rho_p=1200\ \text{kg/m}^3$ being the particle density, μ_f is the dynamic fluid viscosity equal to 2.04×10^{-5} kg/m/s and $Re_p=d_p|\vec{u}-\vec{u}_p|/\nu_f$ the particle Reynolds number. C_c is the Cunningham slip correction factor which accounts for non-continuum effects when calculating the drag on extremely small particles (practically important for $d_p<1\ \mu\text{m}$). It is defined as $C_c=1+\frac{2\lambda}{d_p}[1.257+0.4\exp(-0.55d_p/\lambda)]$, with $\lambda=0.070\ \mu\text{m}$ being the mean free path of air. The drag coefficient C_D is defined as,

$$C_D=\begin{cases}\frac{24}{Re_p}(1+\frac{1}{6}Re_p^{2/3}) & \text{if } Re_p\le 1000\\ 0.44 & \text{if } Re_p>1000.\end{cases} \tag{5}$$

Brownian force is important for very small particles and causes diffusion due to collisions with the air molecules (Finlay, 2001). Its expression is based on the correlation proposed by Li and Ahmadi (1992) given in Eq. (6) (amplitude of the ith component),

$$F_{B,i}=\zeta_i\sqrt{\frac{1}{\tilde{D}}\frac{2K_B^2T^2}{\Delta t}} \tag{6}$$

where ζ_i is a zero mean variant from a Gaussian probability density function, $T=310$ K is the absolute temperature, $\tilde{D}=(k_BTC_c)/(3\pi\mu_f d_p)$ is the Brownian diffusion coefficient, $k_B=1.3806488\times10^{-23}$ m kg/s^2/K is the Boltzmann constant and Δt is the time step for particle equation integration.

The image charge force is the attractive force experienced by a particle with a charge q (in Coulombs) near a conducting wall (Finlay, 2001),

$$\vec{F}_{\text{image}}=\frac{q^2}{16\pi\epsilon_0|\vec{r}_{p,w}|^2}\frac{\vec{r}_{p,w}}{|\vec{r}_{p,w}|}, \tag{7}$$

where $\vec{r}_{p,w}$ is the minimum distance vector between the particle and the conducting wall and $\epsilon_0=8.854\times10^{-12}$ C^2/m^2/N is the permittivity of free space. The unit vector $\vec{r}_{p,w}/|\vec{r}_{p,w}|$ is normal to the wall surface and points away from the space occupied by the air passage. A validation test case for the implementation of the electrostatic image charge force is included in the supplementary material.

The time advancement of the continuous and the dispersed phase are done simultaneously in our simulations: at each time step, the flow equations are solved first in order to obtain the filtered fluid velocity field that is used in the calculation of the drag force and then Eq. (3) is integrated with an implicit Euler scheme. Details regarding the particle tracking algorithm are presented in the supplementary methods. At each time step, 10 particles are released from random positions at the mouth inlet boundary and the injection stops after 120,000 particles of each size have been introduced. The total number and release time of particles was chosen in order to have a sufficient sample and also take into account the time scales of the flow. The initial velocity of the particles is set to match the air velocity at the inlet and hence, differences in the initial momentum of the particles are taken into account when the inlet velocity profile is modified. A particle is considered deposited if the shortest distance from the centre of particle to the airway wall is less than the particle radius. One-way coupling is taken into account assuming dilute particle suspensions.

Particle dimensionless numbers for the main deposition mechanisms, i.e. inertial impaction and electrostatic attraction, are introduced in order to indicate the relative importance between forces acting on a particle. The Stokes number (Stk) is used to measure the relative importance of inertial effects in determining particle trajectories (Finlay, 2001),

$$Stk=\frac{\rho_p d_p^2 U_0 C_c}{18\mu_f D} \tag{8}$$

where U_0 and D are the mean fluid velocity and the local hydraulic diameter of the airway at the current particle location, respectively.

Finlay (2001) proposed a dimensionless parameter to account for the importance of the image charge force $\vec{F}_{image}$,

$$Inc=\frac{C_c}{3\pi U_0 d_p}\frac{q^2}{16\pi\epsilon_0 D^2}\frac{1}{x'^2} \tag{9}$$

where $x'=\frac{x}{D}$ is the nondimensional distance of the particle from the airway wall. The ratio of the above defined dimensionless numbers can be used to determine the relative importance of electrostatic charge effects:

$$\frac{Inc}{Stk}=\frac{3q^2}{8\pi^2U_0^2d_p^3\rho_p\epsilon_0 D}\frac{1}{x'^2}. \tag{10}$$

3. Results and discussion

In this section, simulation results for the effects of the inlet velocity profile, inhalation flowrate and electrostatic charge on particle deposition are presented and discussed. The particle sizes considered in all cases are 0.1, 0.5, 1, 2.5, 5 and 10 μm and the particle density is equal to 1200 kg/m^3.

3.1. Effect of inlet velocity profile

As mentioned previously, two different inlet velocity profiles were considered at a steady inspiratory flowrate of 4.5 l/min. In the first simulation, a uniform velocity profile was set at the extruded mouth inlet of the airway geometry, while in the second simulation, the time averaged values of the measured velocities were applied. The two inlet profiles are shown in Fig. 2.

Fig. 3 displays the contours of the mean velocities in several vertical and horizontal cut-planes, for the two inlet velocity

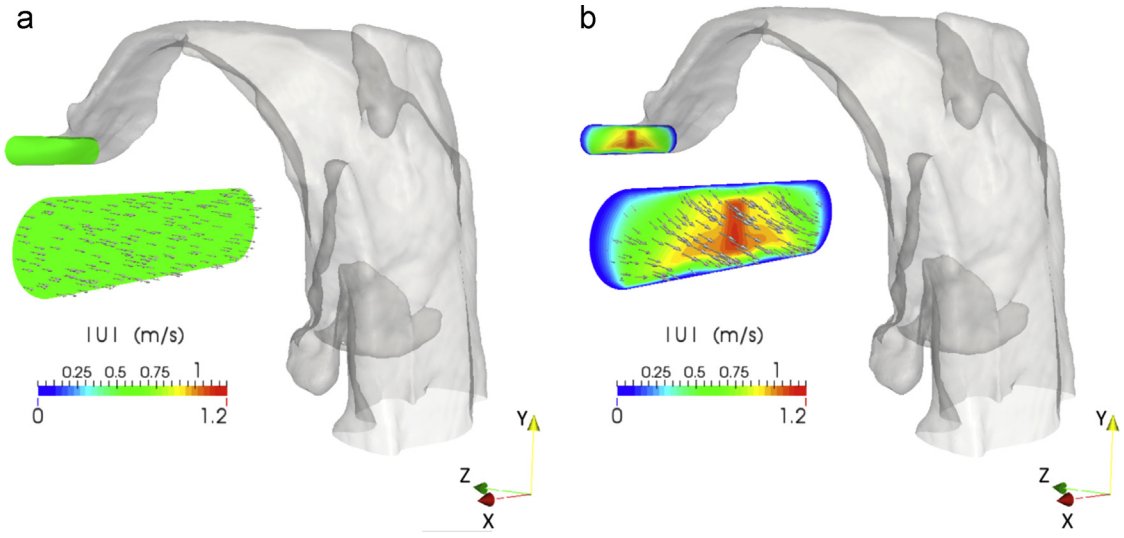

Fig. 2. Different inlet velocity profiles: (a) uniform and (b) LDA-measured.

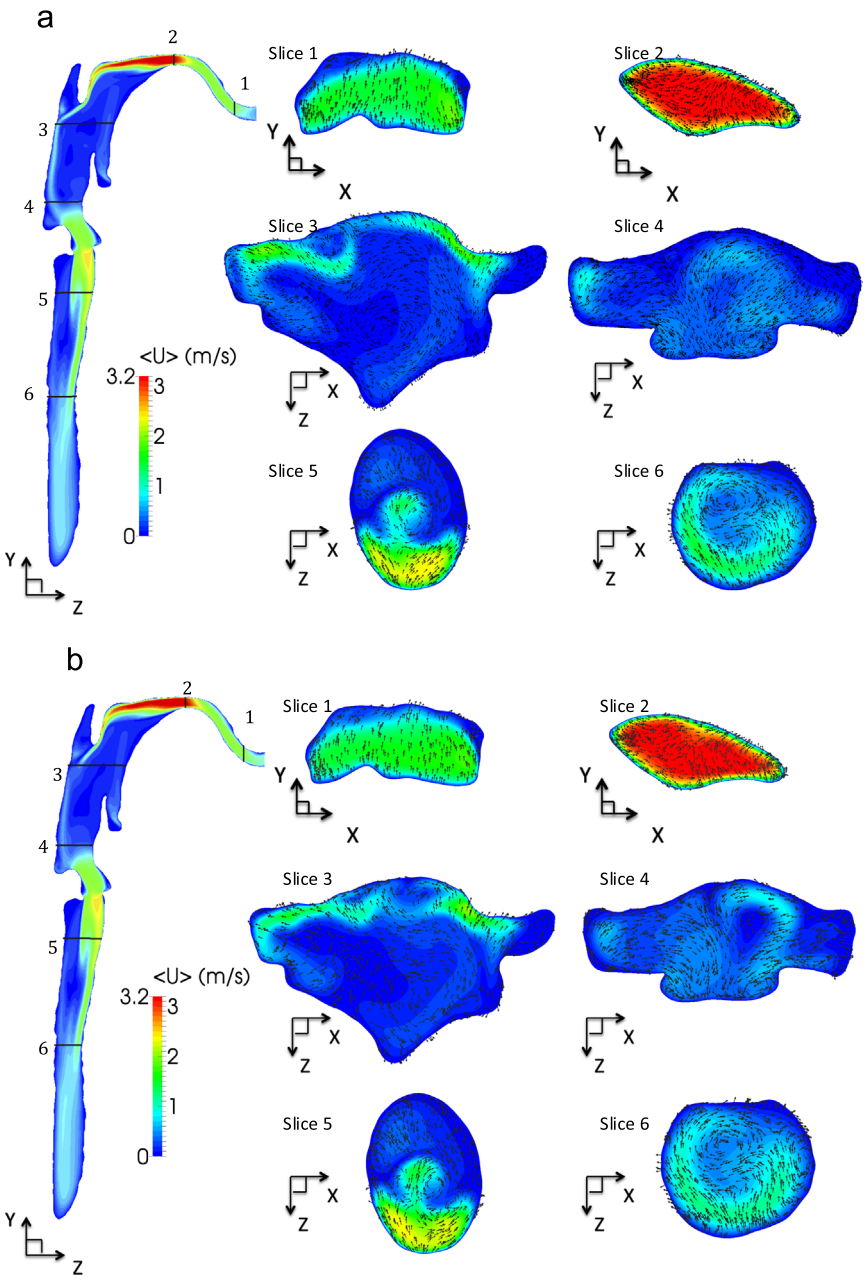

Fig. 3. Contours and vectors of mean velocity for the cases of different inlet velocity profiles (a) uniform and (b) LDA-measured.

conditions. Even in the first cut-plane (slice 1), just a short distance downstream of the mouth inlet, the differences in the initial velocity profiles have been largely smoothed out as a result of geometrical effects. Specifically, the cross sectional area is reduced as we move from the mouth inlet to the oral cavity and therefore the mean velocity accelerates in the region above the tongue and transitions to a more uniform profile. As a result, any upstream flowfield differences dissipate. Surprisingly, some minor differences can be seen in the two cut-planes in the wide passages of oropharynx and laryngopharynx (slices 3 and 4), but most probably these are resulting from having averaged over a relatively small sample for turbulent statistics. Downstream of the glottis constriction the mean velocity fields are identical.

Fig. 4(a) shows the overall DF as a function of particle size, for the two cases considered. As shown, the measured inlet velocity profile corresponds to a higher deposition fraction for all particle sizes. The rise in DF is ranging between 3 and 5%.

In order to investigate the regions with enhanced particle deposition, the upper airway geometry was subdivided into five sub-regions, as shown in Fig. 4(f). The first sub-region consists of the region from the mouth inlet to the end of the first curvature, above the tongue and below the hard and soft palate (referred as tongue). The second sub-region includes the area of the high velocity jet in the oral cavity and extends to the entrance of oropharynx (referred as oral cavity). The third sub-region includes the nasopharynx, oropharynx and extends to the tip of epiglottis (referred as oropharynx), while the fourth sub-region consists of the larynx from the tip of the epiglottis to just below the vocal cords (referred as larynx). The fifth sub-region includes the trachea.

The Deposition Efficiencies (DE, number of deposited particles over the total number of particles that entered the sub-region) were then evaluated for each sub-region (Fig. 4(b)–(f)). Most of the deposition enhancement in the case of the measured inlet velocity occurs in the tongue sub-region, for all particle sizes.

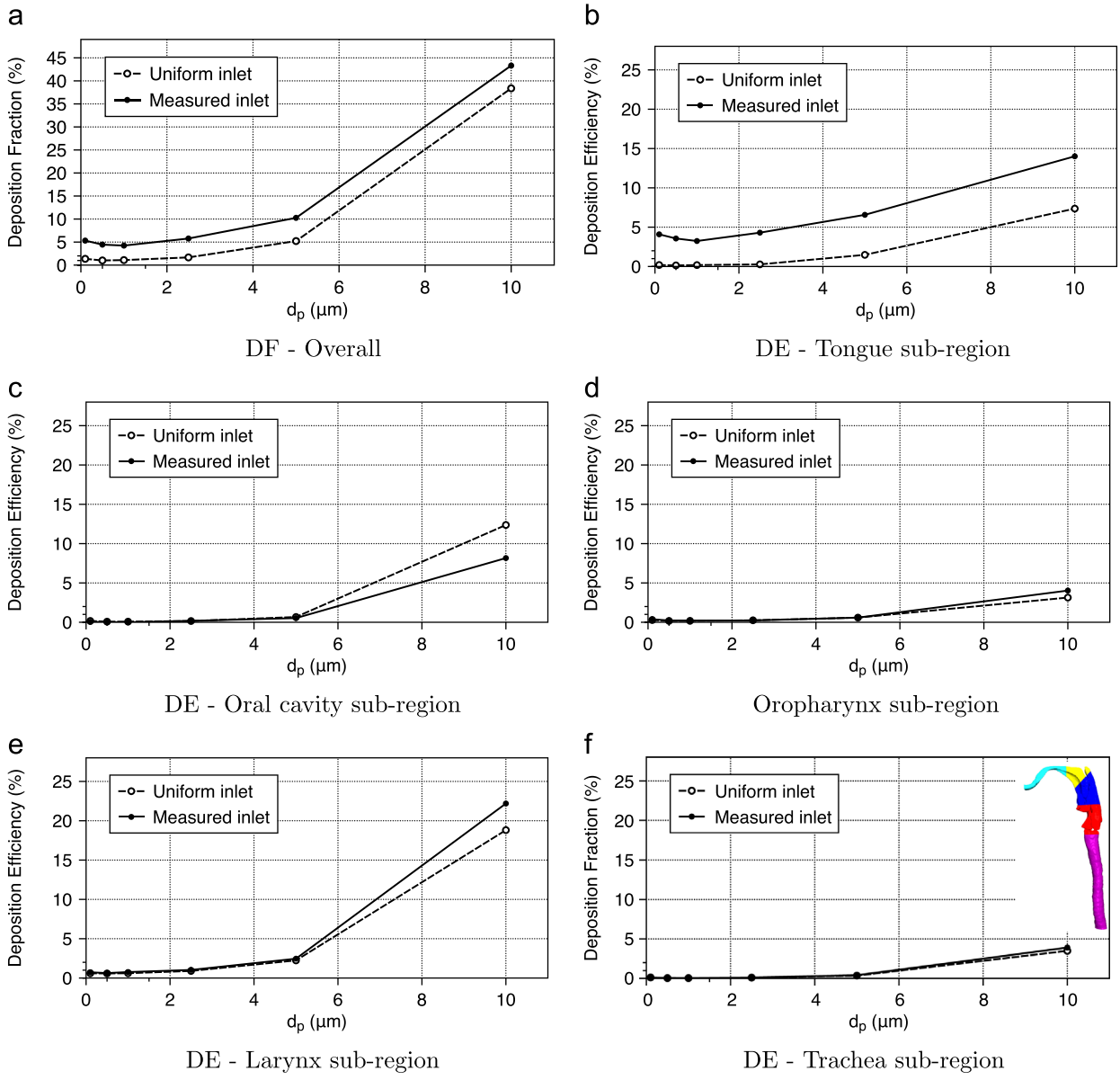

Fig. 4. Modification of deposition as a result of inlet velocity profile. (a) Overall Deposition Fraction, (b)–(f) Deposition Efficiencies in the sub-regions. Sub-regions are shown in (f). Cyan: tongue; yellow: oral cavity; blue: oropharynx; red: larynx; purple: Trachea. (For interpretation of the references to color in this figure caption, the reader is referred to the web version of this paper.)

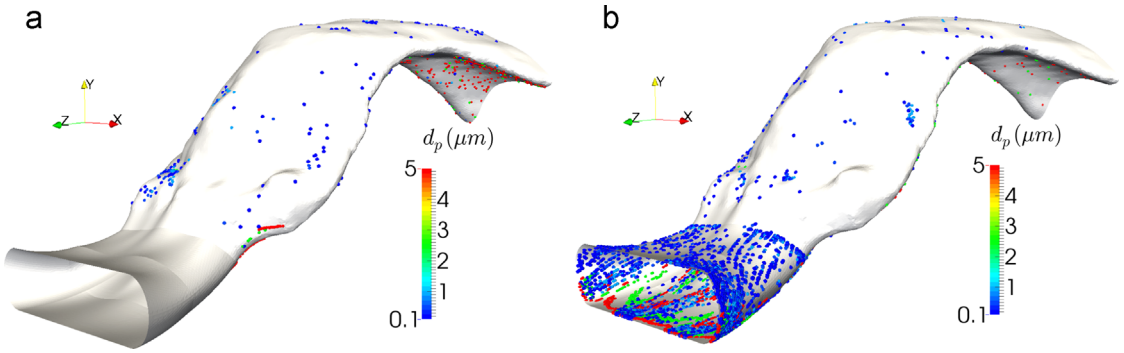

Fig. 5. Deposition locations in the tongue sub-region: (a) uniform velocity profile and (b) measured velocity profile.

For larger particles, the greater deposition is resulting from greater inertial impaction due to higher horizontal velocities and a downward vertical velocity component at the mouth inlet. The downward velocity in conjunction with the upward inclination of the geometry in the tongue region causes larger particles to impinge on the lower walls (tongue), as shown in Fig. 5. In the case of sub-micron particles, Brownian diffusion seems to play a significant role as evidenced by the uniform distribution of the

deposition sites in the region close to the mouth. In the case of LDA-measured inlet conditions, velocities are diminished near the mouth walls (no-slip condition) and this affords particles a longer residence time in the wall proximity. The result is a higher probability of them being deposited due to random motion, at least under these particular flow conditions, i.e. non-uniform inlet velocities and quite low flowrate (4.5 l/min). The region of enhanced deposition has a rather clearly marked downstream border, especially for the sub-micron particles. This corresponds to the location where the geometry transitions from a converging to a diverging shape while undergoing a simultaneous change in curvature.

For particle sizes below 5 μm, the DEs in the subsequent (downstream) sub-regions remain unaffected by the details of the inlet profile. In the case of the largest particles, however, some differences in DE can be observed in the oral cavity and the larynx sub-regions. In the oral cavity, the uniform inlet velocity profile seems to contribute to a higher DE than the measured profile. Apparently, the more efficient filtering of these large particles near the mouth inlet in the case of the measured profile removes some of the particles that, in the case of the uniform inlet profile, manage to escape early deposition and eventually deposit in the oral cavity. In other words, 10 μm particles that as a result of their initial conditions are prone to early deposition are more efficiently filtered out in the tongue sub-region when the measured profile is used; the particles left to enter the oral sub-region are those that are less likely to deposit early.

3.2. *Effect of inhalation flowrate*

In this section, we show the effects of inhalation flowrate (15.2, 30, 60 l/min) on the characteristics of the flowfield and particle deposition in the upper airway geometry (Fig. 1(a)).

3.2.1. *Flowfield*

The inclusion of the lowest inhalation rate (15.2 l/min) allows us to compare and validate our results with those of Choi et al. (2009), who carried a very detailed analysis of the flowfield in the same geometry at this flowrate. The inclusion of the higher flowrates allows us to assess how the flow structure is modified at inhalation rates that can be more relevant to drug delivery.

Fig. 6 shows a side view of the velocity magnitude contours of the normalized mean velocity in a vertical mid-plane of the upper airways. Contours and secondary component vectors are also shown at selected horizontal cut planes (A, B and C). At the lines of intersection of the two planes (vertical and horizontal), the corresponding mean velocity profiles are shown in black color. These results are in good agreement and confirm the observations made by Choi et al. (2009).

Mean flow structures are qualitatively similar for the three flowrates regardless of Reynolds number. The normalized mean velocity initially exhibits a high speed jet in the oral region and then decelerates when passing through the wide and curved passage of the oropharynx and the laryngopharynx. The jet entering the oral cavity causes a recirculation zone close to the anterior wall. The laryngeal jet is formed starting slightly upstream of the glottis due to the constricted cross-sectional area and it impinges on the tracheal front wall. This jetting effect creates a large recirculation zone near the dorsal wall of the upper trachea. Asymmetric counter-rotating secondary motions are generated as we move downstream in the trachea (slices B and C), which agrees well with experimental observations (Johnstone et al., 2004). Further downstream, the jet is dispersed and the secondary motions are weakened.

Fig. 7 shows the contours of normalized TKE in a vertical and three horizontal cut-planes. The results for the lowest inhalation rate (15.2 l/min) are again in good agreement with the study of Choi et al., 2009, but we also note modifications as the flowrate is increased above this value. TKE in the oral region rises rapidly after the constriction due to the soft palate. The location of maximum TKE in this region depends on the Reynolds number. Further downstream in the pharynx, TKE is suppressed due to the increased flow cross-sectional area, but it is augmented again by the glottis constriction. A high TKE region is found at the mixing layer between the cavity-like flow in the recirculation zone and the free stream velocity. A second region of high TKE in the trachea is located near the end of the jet core and is attributable to the transition of the jet to turbulence. These two regions extend in greater areas as Reynolds number is increased. TKE is reduced as we move further downstream to the lower part of the trachea.

Fig. 8 displays the contours of turbulence intensity in a vertical plane cutting through lower trachea and major bronchial airways, at the three flowrates considered. At higher flowrates, higher

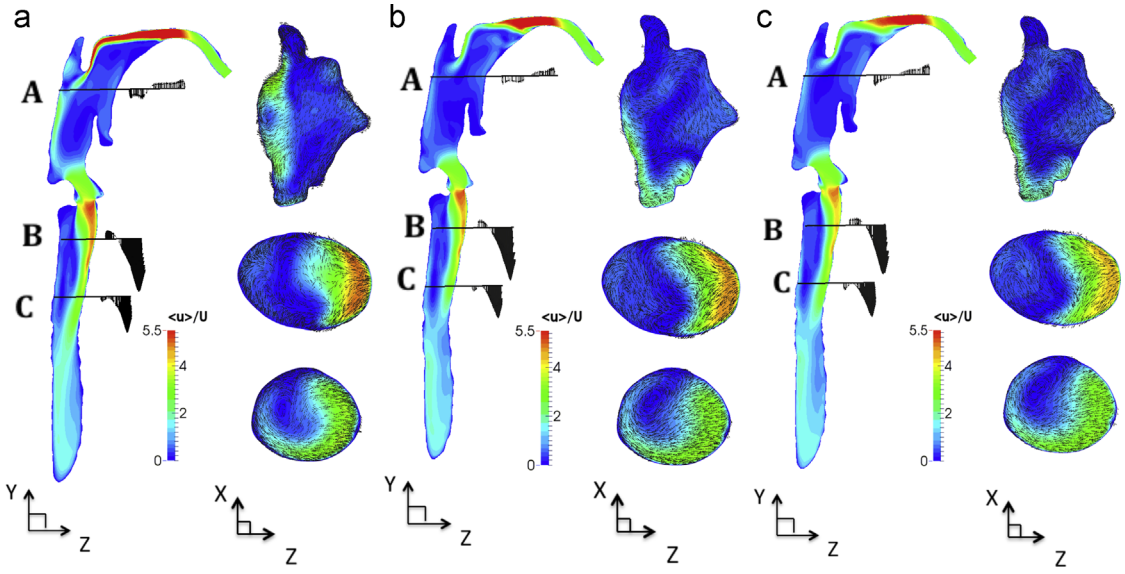

Fig. 6. Contours and vectors of normalized mean velocity. (a) $\dot{Q} = 15.2$ l/min, (b) $\dot{Q} = 30$ l/min, (c) $\dot{Q} = 60$ l/min. The figure is an adaptation of Fig. 5 in Choi et al. (2009) to include the higher flowrates.

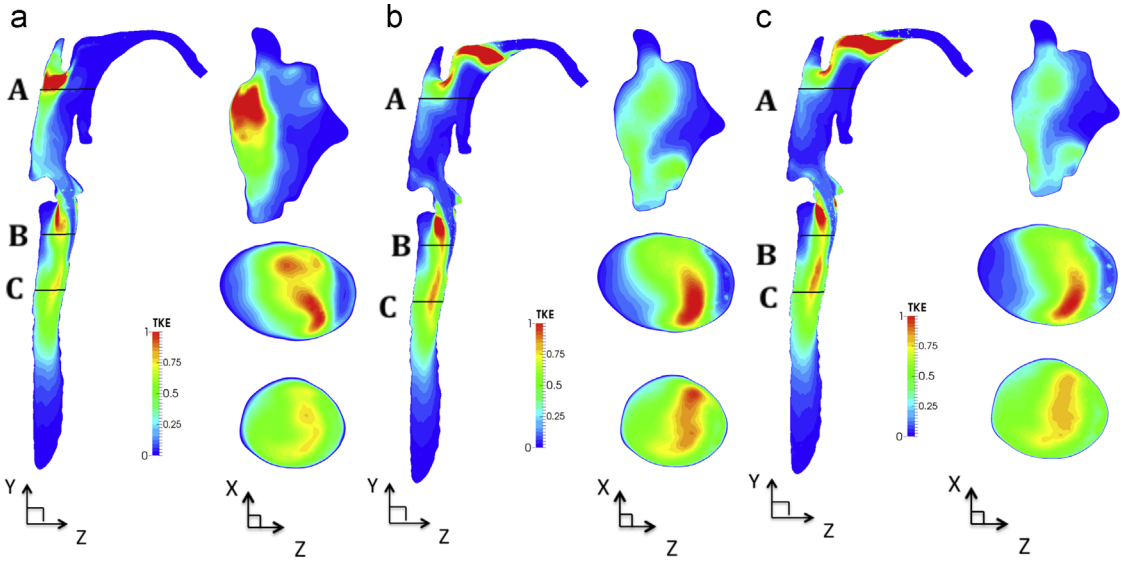

Fig. 7. Contours of normalized turbulent kinetic energy. (a) $\dot{Q} = 15.2$ l/min, (b) $\dot{Q} = 30$ l/min, (c) $\dot{Q} = 60$ l/min. The figure is an adaptation of Fig. 5 in Choi et al. (2009) to include the higher flowrates.

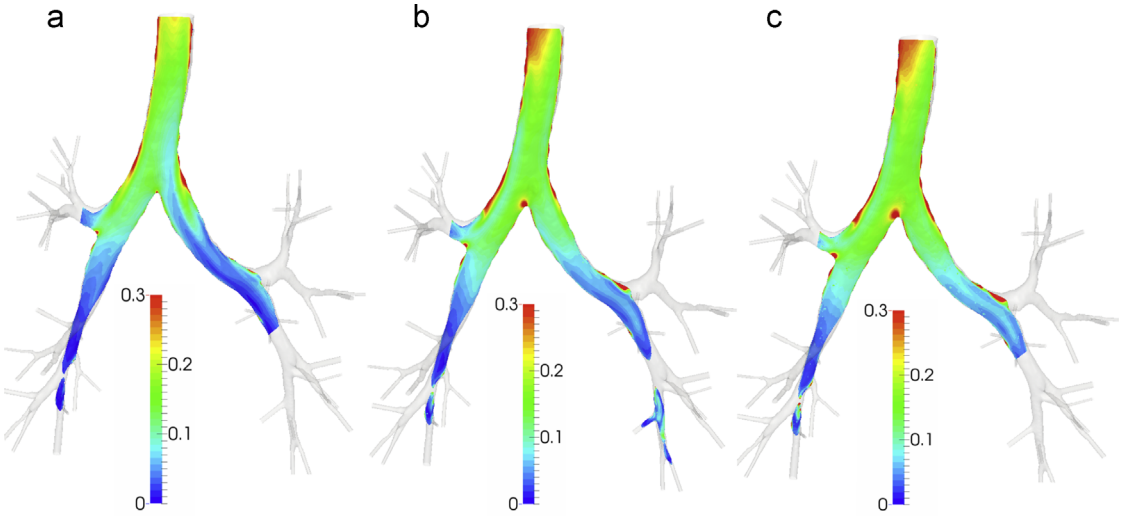

Fig. 8. Contours of turbulence intensity in lower trachea and major bronchial airways. (a) $\dot{Q} = 15.2$ l/min, (b) $\dot{Q} = 30$ l/min, (c) $\dot{Q} = 60$ l/min. The figure is an adaptation of Fig. 20 in Choi et al. (2009) to include the higher flowrates.

values of turbulent intensities are recorded that persist further downstream in the trachea as well as in the main bronchi.

3.2.2. *Particle deposition*

Fig. 9(a), (d) and (g) presents the overall and regional (sub-regions as depicted in Fig. 1(a)) DF of uncharged particles as a function of particle size and flowrate.

Independently of the flowrate, almost all of the 10 μm particles are deposited in the curvatures of the mouth–throat region, as shown in Fig. 9(b), (e) and (h) , due to their high inertia. The effect of flowrate is more pronounced on the deposition of 2.5 and 5 μm diameter particles. Increasing the flowrate from 15.2 to 30 l/min augments the overall DF of 5 μm particles by approximately 40%, while for 2.5 μm particles, increasing the flowrate from 15.2 to 60 l/min causes a rise in overall DF of about 70%. For these particles, the oral jet at the uvula causes significant impaction as shown in Fig. 9(b), (e) and (h). Considerable deposition also occurs on the sidewalls of the larynx immediately upstream of the glottis constriction and on the sidewalls of the upper trachea due to inertial impaction arising from the laryngeal jet and the associated secondary motions (Fig. 9(c), (f) and (i)). Increasing the flowrate causes a similar DF enhancement for the 1 μm particles as well. Brownian diffusion was found to be insignificant compared to the other deposition mechanisms for the cases examined in this section.

The trends described above are consistent with previous studies, such as the mouth–throat deposition experiments of Grgic et al. (2004), who performed measurements in casts of seven oral airway configurations (S1–S5b) at flowrates of 30 and 90 l/min and particle diameters of 3–6.5 μm. Fig. 10 presents the DF in the mouth throat region as a function of Stokes number, based on inlet conditions. In spite of the scattering due to different geometric configuration downstream of the inlet, our result has the same trend as the experimental depositions.

3.3. *Effect of particle charge*

The level of charge on particles depends on the size and physical properties of these aerosols. In the current study five charge levels, i.e. 0, 50, 250, 500 and 1000 elementary charges (e), were

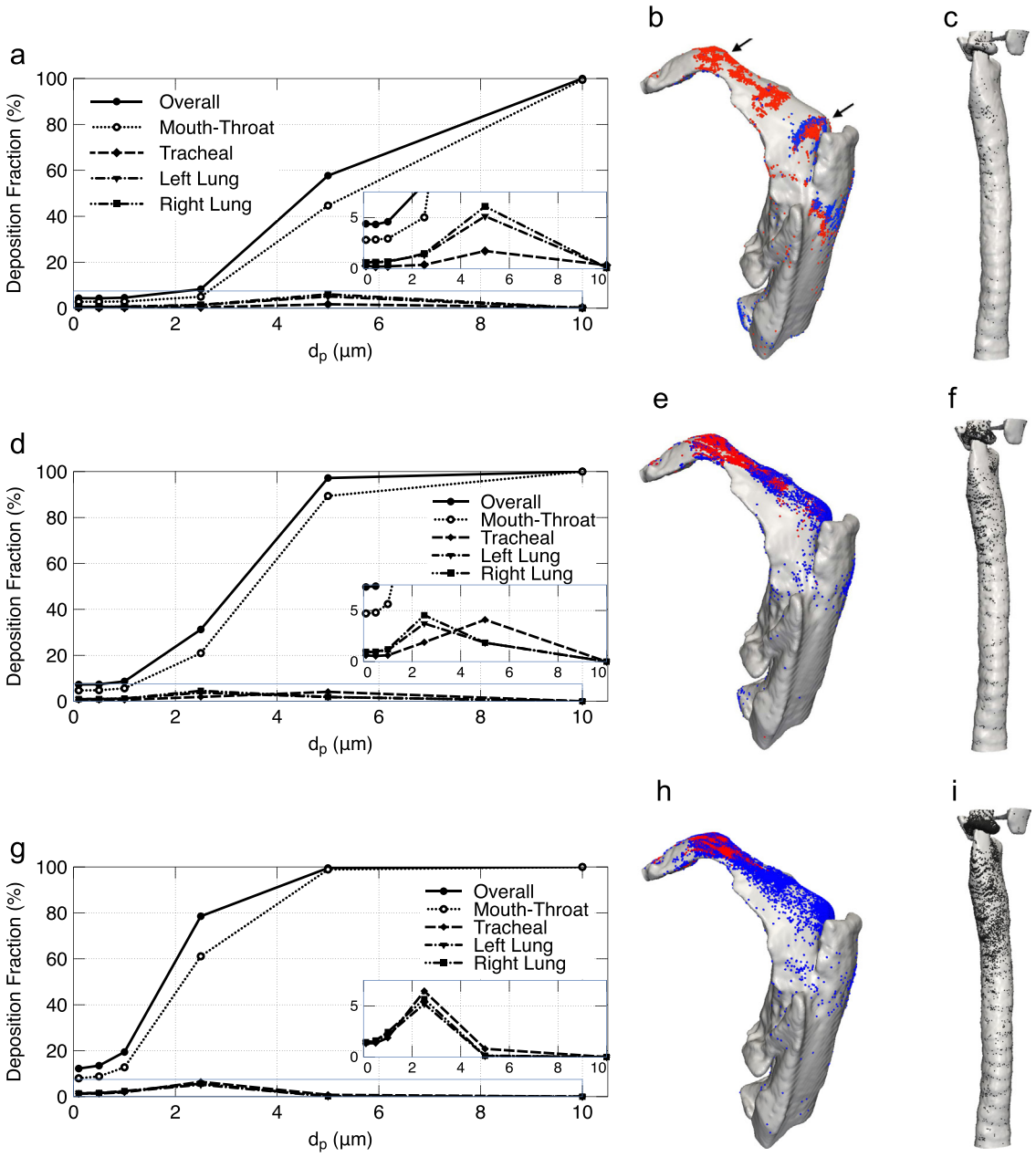

Fig. 9. DF and deposition locations under different flowrates ($q=0$). (a)–(c) $\dot{Q}=15.2$ l/min, (d)–(f) $\dot{Q}=30$ l/min, (g)–(i) $\dot{Q}=60$ l/min. In (b), (e), and (h): blue for $d_p=5$ μm and red for $d_p=10$ μm diameter particles. In (c), (f), and (i): $d_p=2.5$ μm. (For interpretation of the references to color in this figure caption, the reader is referred to the web version of this paper.)

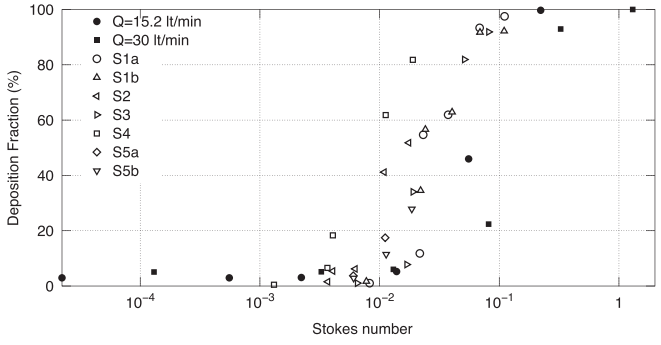

Fig. 10. Comparison of mouth–throat deposition with experimental results of Grgic et al. (2004).

considered. These charge levels are below the Rayleigh charge limit, which is the maximum amount of charge a liquid droplet can carry.

Fig. 11 presents the overall Deposition Fractions (DF) of particles as a function of the particle charge at the three flowrates considered. Note that 5 and 10 μm particles are not shown due to insignificant variation in DF – inertial impaction remains the dominant deposition mechanism for these particles even when charged. Results show considerable increases in overall deposition due to electrostatic effects, especially for smaller particles (the slope of the curves in Fig. 11 increases as the particle size decreases). Specifically, the overall DF of 0.1 μm particles with 1000 elementary charges at a flowrate of 15 l/min is approximately 7 times greater than that with no charge while the

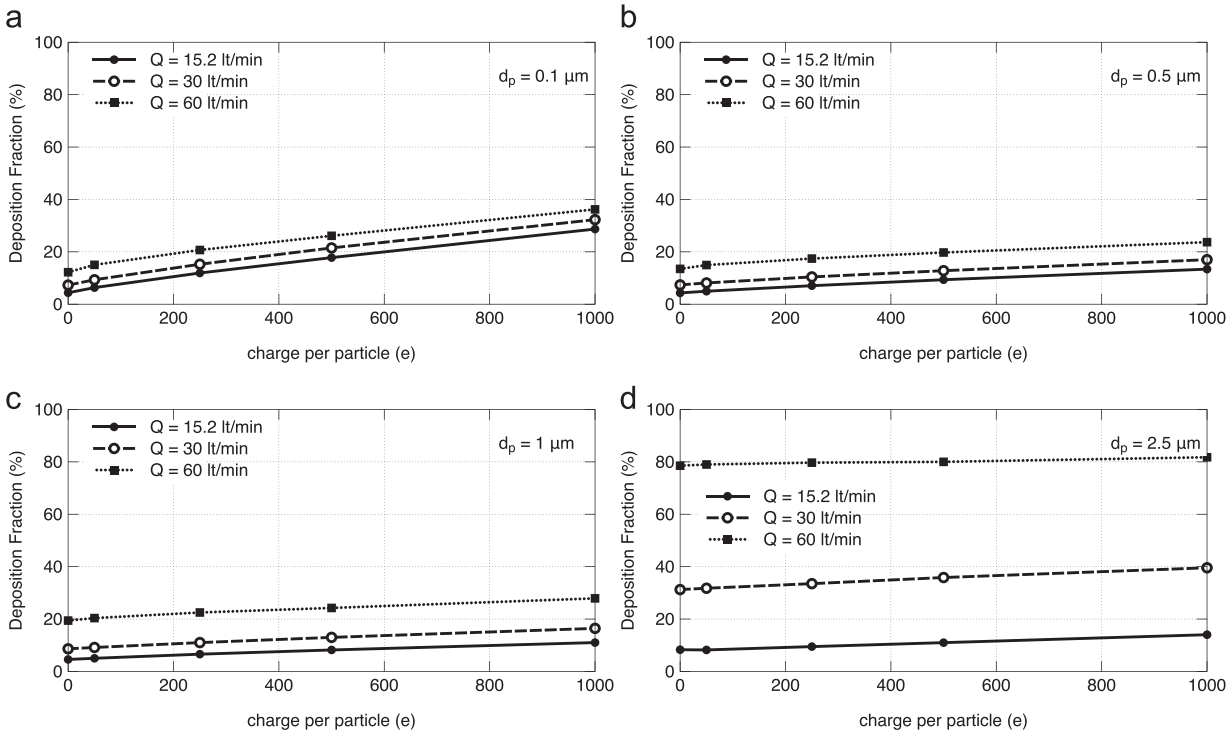

Fig. 11. Overall DF of particles as a function of the electrostatic charge at various flowrates.

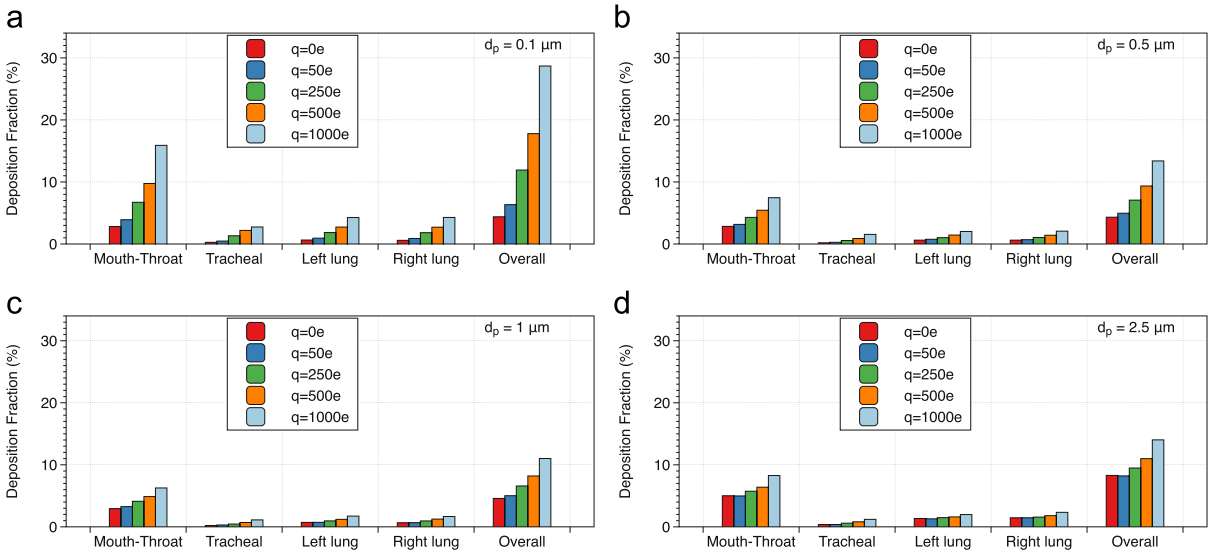

Fig. 12. Overall and sub-regional DF of particles with different charge levels at $\dot{Q} = 15.2$ l/min.

corresponding increase for 2.5 μm particles is 1.5 times. We note that in Eq. (10), the ratio Inc/Stk scales with $1/d_p^3$ and this explains the significantly greater effect of charge on deposition for the smaller particles.

A similar deposition enhancement with increasing charge level is observed at all three flowrates, indicating a relatively small impact of inhalation flowrate on the deposition of charged particles of sizes ranging from 0.1 to 1 μm. However, in the case of 2.5 μm particles, the increase in flowrate dominates the deposition enhancement due to electrostatic charge (DF curve becomes almost horizontal at the highest flowrate of 60 l/min). In other words, these particles are deposited primarily due to inertial impaction and electrostatic precipitation becomes negligible as the flowrate is increased. This agrees qualitatively with Eq. (10), in which the ratio Inc/Stk scales with $1/U_0^2$. The magnitude of mean fluid velocity U_0 in an airway is proportional to the flowrate. Thus, doubling the flowrate causes fourfold decrement of the ratio Inc/Stk and this results in reduced deposition arising from electrostatic attraction compared to impaction.

Bar graphs in Fig. 12 illustrate the overall and sub-regional DFs at a flowrate of $\dot{Q} = 15.2$ l/min (sub-regions shown in Fig. 1(a)). Based on these graphs, most of the deposition enhancement due to electrostatic charge is found to occur in the mouth–throat sub-region. The airway geometry is quite complex in this region including curvature, constrictions, expansions, bifurcating regions and cavities. As a result, the flowfield is also very complex and includes a high velocity jet, recirculation regions, cavity-like flows

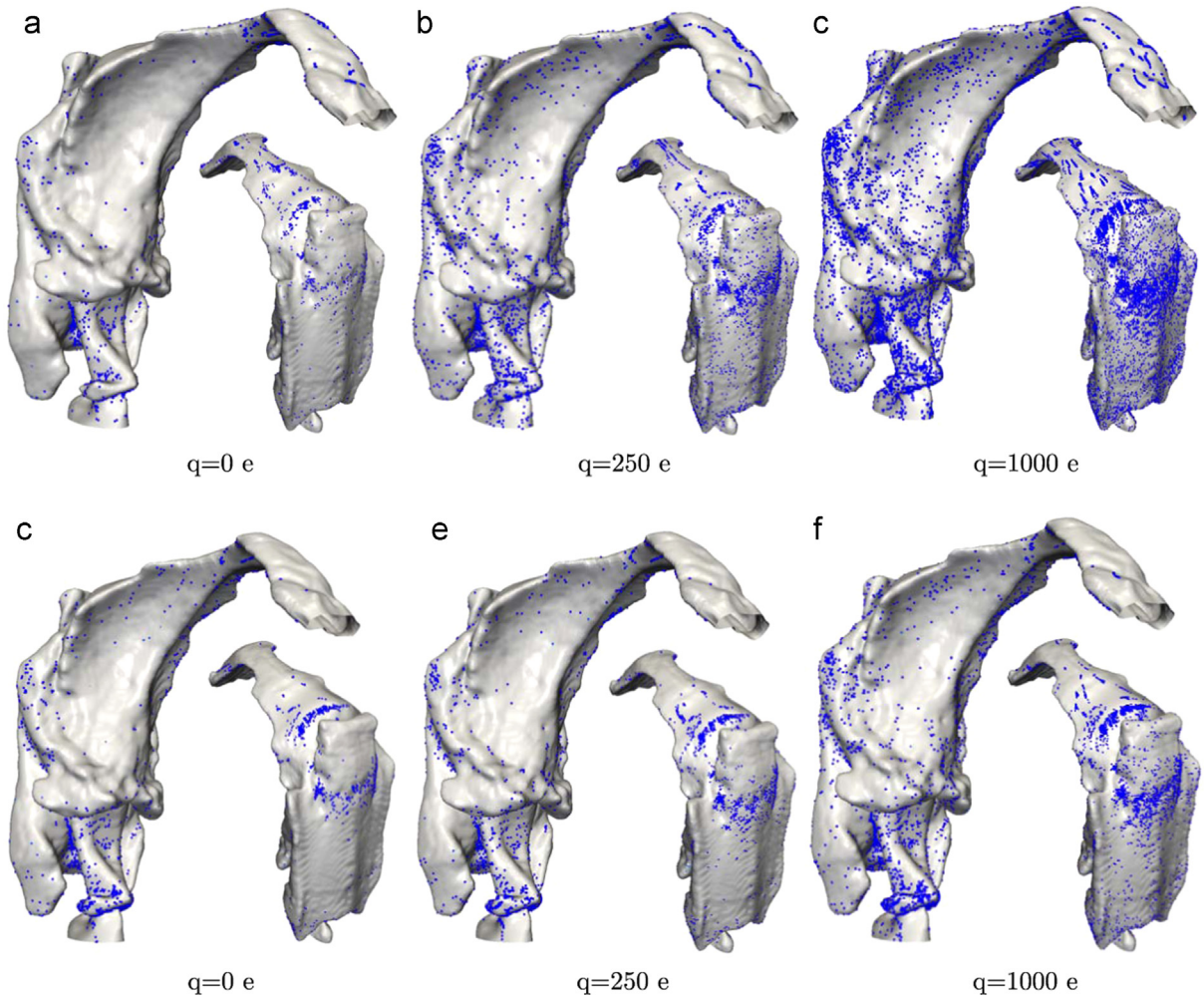

Fig. 13. Deposition locations in the mouth–throat region under different charges ($\dot{Q} = 15.2$ l/min). (a)–(c) 0.1 μm particles, (d)–(e) 2.5 μm particles.

and strong secondary flows. Therefore, correlation of deposition characteristics with particle dimensionless parameters defined previously is not straightforward in the mouth–throat sub-region, since these parameters are more suitable for idealized circular airways. Of course, the effect of charge and particle size on deposition enhancement due to electrostatic effect is still evident, as discussed in the previous paragraph. Furthermore, mouth–throat sub-region constitutes approximately 40% of the total wall surface area. Consequently, the wall surface area that attracts the particles in this region is much larger compared to the other sub-regions. In conjunction with the complex flow characteristics described above, which are likely to bring particles close to the walls, it results in enhanced deposition. Fig. 13 shows the deposition enhancement in the mouth–throat for 0.1 and 2.5 μm diameter particles and electrostatic charges of 0, 250 and 1000e. We observe that deposition is enhanced mostly in regions which already have high deposition due to impaction, namely the rear wall of the oral cavity (marked by the right arrow in Fig. 9(b)) and the rear wall of oropharynx. The uncharged particles follow the fluid streamlines and move close to the airway walls of these two locations. A group of these particles hits the wall and gets deposited while the rest of the particles avoid the collision with the wall. Nevertheless, these particles are still close to the airway walls and if they are charged, they are intercepted by electrostatic attraction. Thus, in these regions electrostatic and inertia effects seem to act synergistically. This is more evident for smaller particles since they are more sensitive to the electrostatic deposition mechanism, as discussed before. Furthermore, deposition of 0.1 μm particles is more evenly dispersed compared to 2.5 μm particles, since smaller particles have lower Stokes number and therefore they are more influenced from secondary flows and turbulent velocity fluctuations.

In general, high mouth–throat deposition of inhaled aerosols is not desirable for therapeutic purposes since the target sites in this case are usually the central conducting airways or the alveolar region of the deep lung. Therefore, care must be taken when assessing the inhaled drug dose of aerosol formulations carrying electrostatic charges. On the other hand, deposition enhancement due to electrostatic effects in the oral airways can act as a filtering mechanism for toxic sub-micron particles that would otherwise be able to penetrate in the deeper lung.

Conducting airways might be primary targets for inhaled drug delivery in local therapies, such as asthma and chronic bronchitis. Based on the bar graphs in Fig. 12, we observe approximately a sevenfold rise in DF in the left and right lung sub-regions (cumulative) for 0.1 μm diameter particles carrying 1000 elementary charges. While the respective DF increases for 0.5 and 1 μm particles are much lower, they still amount to over 200%. Thus, electrostatic charge increases substantially deposition in the conducting airways, especially for sub-micron particles. As indicated by the dimensionless parameter Inc. Eq. (9), the increase in deposition due to electrostatic attraction in the deeper conducting airways is expected to be more pronounced since airway diameter (D) and mean fluid velocity (U_0) decrease in these airways.

3.4. Conclusions

Large Eddy Simulations (LES) were used to investigate deposition of inhaled aerosol particles in a realistic geometry of the human lungs reconstructed from CT-scans. The effects of inlet velocity profile, inhalation flowrate and aerosol charge on particle deposition were examined.

The effect of the inlet velocity profile on the downstream flowfield dissipates quickly as a result of the complex geometry. Although the mean velocity fields are almost identical even at small distances from the mouth inlet, the number of deposited particles is increased in the case of measured velocity inlet conditions. Larger particles with greater inertia impact at the tongue as a result of their higher initial velocities while sub-micron particles are deposited uniformly due to diffusion in the same region. The DEs in the subsequent sub-regions are the same for particle sizes below 5 μm, while for 10 μm some differences occur in the oral cavity and the larynx.

The mean flow structures at the three flowrates are qualitatively similar regardless of Reynolds number. Greater values of turbulent intensities persist more downstream in the trachea and the main bronchi. The Deposition Fraction (DF) of particles is increased with flowrate due to greater inertial impaction, especially for 2.5 and 5 μm diameter particles (enhanced deposition in the mouth–throat region), while 0.1, 0.5 and 1 μm diameter particles have similar DF at a given flowrate.

The effect of charge is more significant for smaller particle sizes; the overall DF of 0.1 μm with 1000 elementary charges is approximately 7 times greater than that with no charge. The impact of inhalation flowrate on the deposition of charged particles is negligible for $d_p \leq 1$ μm, while for $d_p \geq 2.5$ μm inertial impaction prevails over electrostatic deposition mechanism. Deposition enhancement due to electrostatic effects is located mostly in the mouth–throat sub-region due to the large wall surface area that attracts the particles and the complex flowfield found in that region. Considerable increases in deposition of submicron particles are also found in the left and right lung subregions of our geometry, suggesting electrostatic charge manipulation as a possible mechanism for increasing deposition in the conducting airways of the respiratory tree. This could be beneficial in the treatment of diseased airways with inhaled medicines. Further future studies on the topic are therefore recommended.

Conflict of interest statement

The authors declare no conflict of interest.

Disclaimer

The content of this article is the authors' responsibility and neither COST nor any person acting on its behalf is responsible for the use, which might be made of the information contained in it.

Acknowledgments

The present study was funded by the European Union 7th framework program HEXACOMM FP7/2007–2013 under Grant agreement no. 315760. In addition, the authors would like to acknowledge the financial support provided by COST-European Cooperation in Science and Technology, to the COST Action MP1404: Simulation and pharmaceutical technologies for advanced patient-tailored inhaled medicines (SimInhale). Professor Ching-Long Lin of the University of Iowa is gratefully acknowledged for sharing with us the realistic human airway tree geometry. The authors would like to gratefully thank Professor Knud Erik Meyer for support during the LDA experiments that were performed at the Technical University of Denmark.

Appendix A. Supplementary data

Supplementary data associated with this paper can be found in the online version at http://dx.doi.org/10.1016/j.jbiomech.2015.11.029.

References

Ali, M., Reddy, R., Mazumder, M.K., 2008. Electrostatic charge effect on respirable aerosol particle deposition in a cadaver based throat cast replica. J. Electrostat. 66, 401–406.
Bailey, A.G., Hashish, A.H., Williams, T.J., 1998. Drug delivery by inhalation of charged particles. J. Electrostat. 44 (1–2), 3–10.
Byron, P., Peart, J., Staniforth, J., 1997. Aerosol electrostatics. I: Properties of fine powders before and after aerosolization by dry powder inhalers. Pharm. Res. 14 (6), 698–705.
Choi, J., Tawhai, M., Hoffman, E., Lin, C.-L., 2009. On intra- and intersubject variabilities of airflow in the human lungs. Phys. Fluids 21, 101901.
Finlay, W.H., 2001. The Mechanics of Inhaled Pharmaceutical Aerosols. Academic Press, New York.
Forsyth, B., Liu, B.Y.H., Romay, F.J., 1998. Particle charge distribution measurement for commonly generated laboratory aerosols. Aerosol Sci. Technol. 28, 489–501.
Grgic, B., Finlay, W.H., Burnell, P.K.P., Heenan, A.F., 2004. In vitro intersubject and intrasubject deposition measurements in realistic mouth–throat geometries. J. Aerosol Sci. 35 (8), 1025–1040.
Johnstone, A., Uddin, M., Pollard, A., Heenan, A., Finlay, W.H., 2004. The flow inside an idealised form of the human extra-thoracic airway. Exp. Fluids 37, 673–689.
Kleinstreuer, C., Zhang, Z., 2010. Airflow and particle transport in the human respiratory system. Annu. Rev. Fluid Mech. 42, 301–334.
Kwok, P.C.L., Glover, W., Chan, H.K., 2005. Electrostatic charge characteristics of aerosols produced from metered dose inhalers. J. Pharm. Sci. 94 (12), 2789–2799.
Lewis, H., Foster, A., Mullan, B., Cox, R., Clark, R., 1969. Aerodynamics of the human microenvironment. The Lancet 293 (7609), 1273–1277.
Li, A., Ahmadi, G., 1992. Dispersion and deposition of spherical particles from point sources in a turbulent channel flow. Aerosol Sci. Technol. 16, 209–226.
Licina, D., Pantelic, J., Melikov, A., Sekhar, C., Tham, K., 2014. Experimental investigation of the human convective boundary layer in a quiescent indoor environment. Build. Environ. 75, 79–91.
Licina, D., Melikov, A., Pantelic, J., Sekhar, C., Tham, K.W., 2015a. Human convection flow in spaces with and without ventilation: personal exposure to floor-released particles and cough-released droplets. Indoor Air 25 (6), 672–682. http://dx.doi.org/10.1111/ina.12177.
Licina, D., Melikov, A., Sekhar, C., Tham, K., 2015b. Transport of gaseous pollutants by convective boundary layer around a human body. Sci. Technol. Built Environ., 1–12.
Lilly, D.K., 1992. A proposed modification of the Germano subgrid-scale closure method. Phys. Fluids A4 (3), 633–635.
Lin, C.-L., Tawhai, M., Hoffman, E., 2013. Multiscale image-based modeling and simulation of gas flow and particle transport in the human lungs. WIREs Syst. Biol. Med. 5, 643–655.
Longest, P.W., Hindle, M., Choudhuri, S.D., Xi, J., 2008. Comparison of ambient and spray aerosol deposition in a standard induction port and more realistic mouth–throat geometry. Aerosol Sci. 39, 572–591.
Luo, H.Y., Liu, Y., 2008. Modeling the bifurcating flow in a ct-scanned human lung airway. J. Biomech. 41 (12), 2681–2688.
Melandri, C., Tarroni, G., Prodi, V., De Zalacomo, T., Formignani, M., 1983. Deposition of charged particles in the human airways. Aerosol Sci. 14 (5), 657–669.
Prodi, V., Mularoni, A., 1985. Electrostatic lung deposition experiments with humans and animals. Ann. Occup. Hyg. 29, 229–240.
Radhakrishnan, H., Kassinos, S., 2009. CFD modeling of turbulent flow and particle deposition in human lungs. In: The 31st Annual International Conference of the IEEE EMBS, Mineapolis, Minnesota, September 2–6, USA, pp. 2867–2870.
Schiller, L., Naumann, Z., 1935. A drag coefficient correlation. Z. Ver. Deutsch. Ing. 77, 318–320.
Tan, F.P., Wood, N.B., Tabor, G., Xu, X.Y., 2011. Comparison of les of steady transitional flow in an idealized stenosed axisymmetric artery model with a RANS transitional model. J. Biomech. Eng. 133 (5), 1001–1012.
Tawhai, M., Lin, C.-L., 2011. Airway gas flow. Compr. Physiol. 1, 1135–1157.
Weibel, E.R., 1963. Morphometry of the Human Lung. Springer-Verlag, Berlin.
Xi, J., Longest, P.W., 2007. Transport and deposition of micro-aerosols in realistic and simplified models of the oral airway. Ann. Biomed. Eng. 35 (April), 560–581.
Yu, C., 1985. Theories of electrostatic lung deposition of inhaled aerosols. Ann. Occup. Hyg. 29, 219–227.